Discovery of high-performance thermoelectric copper chalcogenide using modified diffusion-couple high-throughput synthesis and automated histogram analysis technique

Journal:	*Energy & Environmental Science*
Manuscript ID	EE-ART-07-2020-002209
Article Type:	Paper
Date Submitted by the Author:	13-Jul-2020
Complete List of Authors:	Deng, Tingting; Shanghai Institute of Ceramics Chinese Academy of Sciences; University of the Chinese Academy of Sciences; ShanghaiTech University School of Physical Science and Technology Xing, Tong; Shanghai Institute of Ceramics Chinese Academy of Sciences; University of the Chinese Academy of Sciences Brod, Madison; Northwestern University Sheng, Ye; Shanghai University, Materials Genome Institute Qiu, Pengfei; Shanghai Institute of Ceramics Chinese Academy of Sciences; University of the Chinese Academy of Sciences Veremchuk, Igor; Helmholtz-Zentrum Dresden-Rossendorf, Institute of Ion Beam Physics and Materials Research Song, Qingfeng; Shanghai Institute of Ceramics Chinese Academy of Sciences; University of the Chinese Academy of Sciences Wei, Tian-Ran; Shanghai Jiao Tong University, School of Materials Science and Engineering Yang, Jiong; Shanghai University, Materials Genome Institute Snyder, G.; Northwestern University, Materials Science Grin, Yuri; Max-Planck-Institut für Chemische Physik fester Stoffe, Chemical Metals Science Chen, Lidong; Shanghai Institute of Ceramics Chinese Academy of Sciences; University of the Chinese Academy of Sciences Shi, Xun; Shanghai Institute of Ceramics Chinese Academy of Sciences

Table of Contents Entry

A modified HTP synthesis method and an automated histogram analysis technique are developed to screen the new stable ternary CTS compound $Cu_7Sn_3S_{10}$.

Reducing greenhouse gas emissions has become an important task for the world. Thermoelectric technology can more efficiently use fossil energy by converting industry and vehicle exhaust waste heat into useful electricity, providing an alternative way to reduce greenhouse gas emissions. Advanced thermoelectric technology requires high-performance thermoelectric materials with earth-abundant and environmentally friendly elements. However, the state-of-the-art thermoelectric materials usually consist of expensive or toxic elements (e.g. Ge, Te, or Pb). Thus, searching new high-performance thermoelectric materials that are economical and environmentally friendly is an urgent task for thermoelectric society, but the advancements are greatly limited by the traditional trial-and-error method. Herein, following the Materials genome initiative, we propose a high-throughput synthesis method and an automated histogram analysis technique to quickly screen high-performance new thermoelectric materials. Taking economical and environmentally friendly Cu-Sn-S ternary system as a case study, a new copper chalcogenide with the composition of $Cu_7Sn_3S_{10}$ is discovered and found to possess high thermal stability, low lattice thermal conductivity, and decent electrical transports. The peak of its thermoelectric figure of merit reaches 0.8 at 750 K, being among the highest values reported in Cu-Sn-S ternary materials.

Discovery of high-performance thermoelectric copper chalcogenide using modified diffusion-couple high-throughput synthesis and automated histogram analysis technique

Tingting Deng, [abc] Tong Xing, [ab] Madison Brod, [d] Ye Sheng, [e] Pengfei Qiu,*[ab] Igor Veremchuk, [f] Qingfeng Song, [ab] Tian-Ran Wei, [g] Jiong Yang, [ae] G. Jeffrey Snyder,*[d] Yuri Grin, [h] Lidong Chen [ab] and Xun Shi*[a]

Discovery of novel high-performance materials with earth-abundant and environmentally friendly elements is a key task for civil applications based on advanced thermoelectric technology. Advancements in this area are greatly limited by the traditional trial-and-error method, which is both time-consuming and expensive. The materials genome initiative can provide a powerful strategy to screen for potential novel materials using high-throughput calculations, material characterization, and synthesis. In this study, we developed a modified diffusion-couple high-throughput synthesis method and an automated histogram analysis technique to quickly screen high-performance copper chalcogenide thermoelectric materials, which has been well demonstrated in the ternary Cu-Sn-S compounds. A new copper chalcogenide with the composition of $Cu_7Sn_3S_{10}$ was discovered. The study on crystal structure, band gap, and electrical and thermal transport properties, were performed to show that it is a promising thermoelectric material with ultralow lattice thermal conductivity, moderate band gap, and decent electrical conductivity. Via Cl doping, the thermoelectric dimensionless figure of merit zT reaches 0.8 at 750 K, being among the highest values reported in Cu-Sn-S ternary materials. The modified diffusion-couple high-throughput synthesis method and automated histogram analysis technique developed in this study also shed light on the development of other advanced thermoelectric and functional materials.

Introduction

Materials genome initiative provides the means to reduce the cost and development time of materials discovery, optimization, and development, launching the material science into a new era. High-throughput (HTP) calculations, material characterizations, and synthesis, are the essential components of this approach.[1, 2] In recent years, HTP calculations based on the data-driven approach and machine learning method have achieved great success in recognizing new functional materials from the ~40,000 known crystalline materials in the Inorganic Crystal Structure Database (ICSD).[3-6] HTP characterization has also demonstrated advantages in immensely decreasing the

time of characterization.[7-10] Likewise, HTP synthesis has potential for quickly screening the optimized chemical composition corresponding to the best properties for the known functional materials. However, applications of HTP synthesis to develop hitherto unknown functional material are still very rare.

Copper chalcogenides have been extensively studied in various fields, such as thin-film solar-cell materials, optics, electrochemistry, biology, functional coatings, and gas-sensing technology.[11-15] Recently, investigations on copper chalcogenides have been extended to the field of thermoelectrics.[16, 17] Thermoelectric (TE) technology is a clean and renewable energy source which can convert waste heat into useful electricity.[18] With the increasing concern on the energy crisis and environmental pollution, TE technology is attracting more and more attention in both academic and industry communities.[19, 20] However, most current state-of-the-art TE materials consist of toxic, expensive, or scarce elements (e.g., Pb, Te, Ge, Yb, or Co), limiting the use of TE technology in civil applications. Thus, the search of novel high-performance TE materials consisting of eco-friendly, earth-abundant elements has become a hot topic in the TE community.[21] Towards this goal, the copper chalcogenides with good TE performance, *e.g.* Cu_2X (X = S/Se/Te)[22, 23], $Cu_{12}Sb_4S_{13}$[24], and $CuAgSe$[25], have attracted great attention. Among various chalcogenides, Cu-Sn-S (CTS) ternary compounds are a novel class of TE materials. So far, there are four CTS ternary compounds which have been reported with decent TE performance, which are Cu_2SnS_3[26, 27],

a. State Key Laboratory of High Performance Ceramics and Superfine Microstructure, Shanghai Institute of Ceramics, Chinese Academy of Sciences, Shanghai 200050, China. E-mail: xshi@mail.sic.ac.cn, qiupf@mail.sic.ac.cn
b. Center of Materials Science and Optoelectronics Engineering, University of Chinese Academy of Sciences, Beijing 100049, China.
c. School of Physical Science and Technology, Shanghai Tech University, Shanghai 201210, China.
d. Department of Materials Science and Engineering, Northwestern University, Evanston, Illinois 60208, USA. E-mail: jeff.snyder@northwestern.edu
e. Materials Genome Institute, Shanghai University, Shanghai 200444, China.
f. Helmholtz-Zentrum Dresden-Rossendorf, Institute of Ion Beam Physics and Materials Research, 01328 Dresden, Germany.
g. State Key Laboratory of Metal Matrix Composites, School of Materials Science and Engineering, Shanghai Jiao Tong University, Shanghai 200240, China.
h. Max-Planck-Institut für Chemische Physik fester Stoffe, Dresden, Germany.
† Electronic Supplementary Information (ESI) available. See DOI: 10.1039/x0xx00000x

Cu_3SnS_4[28], Cu_4SnS_4[29], and $Cu_4Sn_7S_{16}$[30, 31]. Among them, Cu_2SnS_3 with Co element as a dopant displays the maximum, thermoelectric figure of merit, *zT,* of 0.85 at 723 K, showing a great potential to be used in civil applications.[27]

Other CTS ternary TE compounds, such as Cu_3SnS_4, $Cu_{10}Sn_2S_{13}$, $Cu_{9.67}Sn_{2.33}S_{13}$, $CuSn_{3.75}S_8$, $Cu_2Sn_4S_9$, Cu_4SnS_6, Cu_8SnS_6, $Cu_2Sn_3S_7$, $Cu_2Sn_{3.34}S_{7.6}$, $Cu_{10}Sn_2S_{13}$, $Cu_2Sn_2S_5$, Cu_5SnS_4, Cu_5SnS_6, $Cu_4Sn_3S_8$, $Cu_5Sn_2S_7$, $Cu_7Sn_3S_{10}$, $Cu_2Sn_2S_9$, $Cu_8Sn_3S_{12}$, and $Cu_9Sn_2S_9$, have been also mentioned in the literature.[32] Some of them might also be potentially promising TE materials, but choosing an appropriate one is quite difficult because the crystal structures, physical properties and chemical properties of most of them are not well understood. Particularly, the phase stability ranges are still controversial. For example, Moh *et al.* reported the existence of $Cu_2Sn_2S_5$ and Cu_5SnS_4, while Wang *et al.* suggested that they do not exist. Furthermore, Wang *et al.* reported the existence of $Cu_2Sn_3S_7$, while Sobott *et al.* described that $Cu_2Sn_{3.5}S_8$ rather than $Cu_2Sn_3S_7$ is the stable phase. Khanafer *et al.* reported a CTS ternary compound $Cu_4Sn_3S_8$, which is discarded by Piskach *et al.* but confirmed by Fiechter *et al.*[33] Large amounts of time and resources would be consumed if the traditional serial ("artisanal") technique continues to be adopted to synthesize the compounds one by one and determine the stable phase. Thus, it is necessary to develop a new HTP synthesis method to quickly screen the CTS ternary compounds for thermoelectric applications.

In this study, a modified diffusion-couple HTP synthesis method and an automated histogram analysis technique are developed to screen for and discover the new stable ternary CTS compound $Cu_7Sn_3S_{10}$ with ultralow lattice thermal conductivity and good TE figure of merit *zT* up to 0.8 at 750 K, which is among the highest values reported in Cu-Sn-S copper chalcogenides. Based on the effective mass model, an even higher *zT* of 1.1 is attainable at 750 K by further decreasing the carrier concentration.

Results and discussion

The diffusion-couple method is an important and efficient tool for determining a material's phase diagram, especially the high-temperature isothermal sections.[34, 35] In this work, we developed a modified diffusion-couple HTP synthesis method by mixing two binary reactants together and annealing them at given high temperatures to ensure sufficient diffusion of atoms. In this way, multiple stable phases will form in a single sample to reach the local equilibrium at given temperatures. Then, we can quickly find the novel stable phases through analyzing these individual samples.

As a case study, we applied this modified diffusion-couple HTP synthesis method to screen and discover the new stable ternary CTS compounds. Since many CTS compounds (*e.g.* Cu_2SnS_3, Cu_3SnS_4, $Cu_5Sn_2S_7$, $Cu_7Sn_3S_{10}$, Cu_4SnS_6, $Cu_2Sn_2S_5$, $Cu_2Sn_{3.34}S_{7.6}$, Cu_5SnS_4, Cu_5SnS_6, $Cu_4Sn_3S_8$, $Cu_8Sn_3S_{12}$ and $Cu_{10}Sn_2S_{13}$) have chemical compositions around the CuS-SnS line, we chose the pre-synthesized binary CuS and SnS compounds as the reactants for performing the modified diffusion-couple HTP synthesis (Fig. 1). The mixtures of CuS and SnS powders, with nine different mole ratios from 10:90 to 90:10, were loaded into the graphite die in sequence and then spark-plasma sintered at a temperature of 700 K for 15 min to be consolidated into a bulk sample. The sintered nine-segment bulk sample was annealed at 700 K for 3 days to promote the reaction between CuS and SnS forming CTS compounds. Further details can be found in Experimental section.

The microstructure of the annealed nine-segment bulk sample cut along the direction of the sintering pressure is shown in Fig. 2a and 2b. It should be noted that none of the segments contains pure single phase only because the component elements cannot sufficiently diffuse during the first 3 days of the annealing process. However, aside from the initial reactants and the pores with black contrast, many areas with new contrasts between those of CuS and SnS appear, proving the formation of CTS compounds. The microstructure and phase composition evolutions inside each segment are very complex (Fig. 2b).

In order to give an unbiased and high-speed analysis on the BSE images, an automated histogram analysis technique is developed. Basically, this method adopts the greyscale histograms of the BSE images, and identifies the phases with highest frequencies in the summed histogram. Three procedures are included: 1) image segment by Otsu threshold method[36] to filter out the background including a large amount of holes and rough areas, as shown in Fig. 2c, 2) calibration of the brightness by one of the parent phases SnS in the greyscale histograms, and 3) summation of the calibrated greyscale histograms, as shown in Fig. 2d. The one with the highest
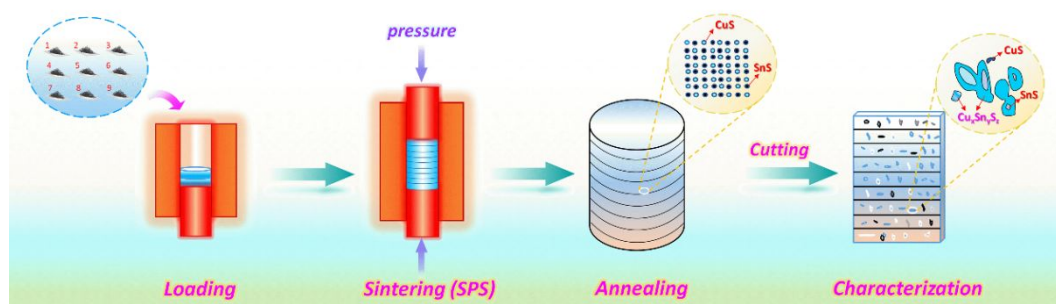

Fig. 1 Scheme of the modified diffusion-couple HTP synthesis method to screen and discovery the new CTS TE compounds.

frequency in Fig. 2d is the parent phase SnS. The other parent phase CuS has been directly filtered out in the first procedure because it is prone to locate at porous areas. Thus, there is no peak that is related to CuS in Fig. 2d. There are two greyscale peaks in the intermedium range, indicating two CTS ternary phases. The Energy Dispersive X-ray Spectroscopy (EDS) analysis shows that one of the CTS ternary phases is the known Cu_2SnS_3. Notably, the composition of the other phase shown in Fig. 2d is $Cu_7Sn_3S_{10}$. This result suggests that Cu_2SnS_3 and $Cu_7Sn_3S_{10}$ are more likely to form compared with other CTS ternary compounds.

In the present modified diffusion-couple HTP synthesis, furnace-cooling was performed after the sintered nine-segment bulk sample was annealed at 700 K for 3 days to achieve possible stable thermodynamic phases. This is different from the more common method of studying the phase diagram, in which the compositions determined are usually obtained by quenching the material from high temperatures. This seems to be a key reason why many reported CTS compounds are controversial, as they are metastable phases at room temperature. Thus, based on the observation in our experiment, Cu_2SnS_3 and $Cu_7Sn_3S_{10}$ should be thermodynamically stable at room temperature. Cu_2SnS_3 is a known compound that is included by the ICSD. However, composition $Cu_7Sn_3S_{10}$ is not known in the ICSD. It was only proposed by Wang *et al* in 1977, and mentioned by Wu *et al* in 1986 and Fiechter *et al.* in 2003,[32, 33] but its crystal structure, thermal stability, and physical properties have never been reported.

In order to investigate the CTS compound discovered by the modified diffusion-couple synthesis, $Cu_7Sn_3S_{10}$ was synthesized by melting-annealing-ball milling method (with the preparation details described in Experiment section). All elements, Cu, Sn, and S, are homogeneously distributed in the sample (Fig. 3a). The chemical composition is determined through energy dispersive spectroscopy (EDS) as $Cu_{34.7\pm0.5}Sn_{15.2\pm0.8}S_{50.1\pm0.4}$, being consistent with the nominal chemical composition. The high-temperature stability of the prepared $Cu_7Sn_3S_{10}$ was tested by the thermogravimetric (TG)/differential thermal analysis (DTA)
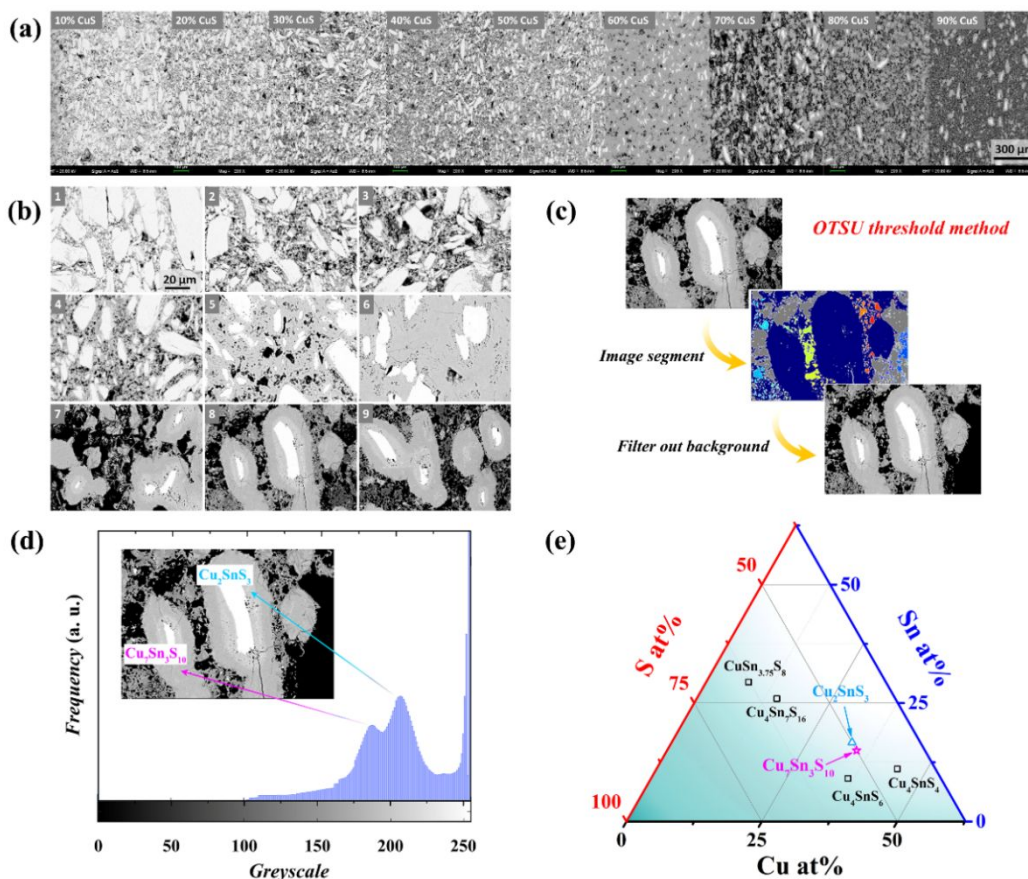

Fig. 2 (a) Backscattered electron (BSE) images for the cross-section of the annealed nine-segment bulk sample cut along the direction parallel to the sintering pressure. (b) BSE images under larger magnification performed on each segment. The areas with the grayest contrast are CuS and the areas with the brightest contrast are SnS. The areas with contrasts between them are CTS ternary compounds. The areas with black contrast are pores. (c) Process of images pretreatment for nine BSE images. (d) Summation of the calibrated greyscale histograms on the nine BSE images shown in (b). (e) Gibbs phase triangle for the Cu-Sn-S system. Two stable CTS ternary compounds, Cu_2SnS_3 and $Cu_7Sn_3S_{10}$, determined by the automated histogram analysis technique

and Energy Dispersive X-ray Spectroscopy (EDS), are plotted in the Gibbs phase triangle. Other CTS ternary compounds included in ICSD are also plotted.

analyses. No obvious mass loss is observed until 750 K, indicating that the sulfur in $Cu_7Sn_3S_{10}$ is stable with a low volatilization rate (Fig. 3b). In addition, an endothermic peak appears around 350 K in the DTA curve. This suggests that $Cu_7Sn_3S_{10}$ has a phase transformation around this temperature. However, the collected X-ray diffraction patterns above 400 K have no obvious difference with that at 300 K (Fig. 3c). Thus, this phase transformation is expected to be caused by the Cu order-disorder transition rather than the change of structure symmetry. Similar phenomenon has been also observed in many Cu-based diamond-like compounds with tetragonal structures, such as $Cu_2ZnGeSe_4$[37, 38] and $Cu_2(Mn/Fe/Co)SnSe_4$[39]. At certain temperature, the thermal energy can overcome the bonding attraction between the copper ions and the anions yielding the Cu disorder, such as interstitial occupancy of copper or even mobile Cu, which might be responsible for the phase transformation shown in Fig. 3b.[38]

The powder X-ray diffraction pattern of $Cu_7Sn_3S_{10}$ prepared by melting-annealing-ball milling method is similar to the cubic sphalerite one but contains additional reflections (Fig. 4a). All reflections were successfully indexed in the tetragonal stannite-like unit cell with $c \approx 2a$. Assuming $2a$, $2b$, and $4d$ sites occupied by Cu and Sn (cationic sites) and $8i$ site only occupied by S (anionic site), the refinement of the crystal structure using the powder diffraction data (5000 point intensities and 152 independent reflections in the measured 2θ range) yields acceptable residual values and atomic displacement parameters (model 1, Table S1), but the so-obtained composition $Cu_{39.3}Sn_{10.7}S_{50.0}$ is far from the nominal one $Cu_{35}Sn_{15}Sn_{50}$, which is confirmed also by EDS analysis. An attempt to fix the occupancies of the cationic positions based on the nominal composition of the material yields practically the same residual

values but large spread of the atomic displacement parameters (model 2, Fig. 4a, Table 1). Furthermore, the model which yields the expected chemical composition, shows reasonable values of the atomic displacement parameters, and fits well the experimental data (model 3, Table S2), requires to assume mixed cation/anion occupancies of the positions within the space group $I\bar{4}2m$. The clarification of this issue is the topic of separated study and is beyond the scope of this paper. For the following investigation, the model 2 is used. The detailed crystallographic information is shown in Table 2. The structure of $Cu_7Sn_3S_{10}$ is isotypic to the structure of stannite $[Cu_2(Fe,Zn)SnS_4]$[40]. Based on the atomic coordinates and isotropic displacement parameters listed in Table 1, the schematic of its crystal structure is depicted in the inset of Fig. 4a. Each S site is coordinated by one Cu1, one M1, and two M2 sites, forming a three-dimensional network of slightly distorted corner-sharing tetrahedrons. Likewise, each cationic site (Cu1/M1/M2) is coordinated by four S sites. The selected interatomic distances and angles within the cation-centered sulfur tetrahedron were listed in Table S3.

Selected area electron diffraction (SAED) experiments were performed on $Cu_7Sn_3S_{10}$ to further verify the above refined crystal structure. As shown in Fig. 4b, c, clean and clear electron diffraction spots can be found, which match well with the [110] zone axis and [201] zone axis of the tetragonal $Cu_7Sn_3S_{10}$, respectively. The distances of crystal planes (002), $(1\bar{1}2)$ and $(1\bar{1}0)$ in the [110] zone axis are 5.38 Å, 3.12 Å, and 3.75 Å, respectively. The distances of crystal planes $(11\bar{2})$ and (020) in the [201] zone axis are 3.07 Å and 2.67 Å, respectively. These values are consistent with those of the structure parameters determined by the X-ray Rietveld refinement (Table 2), such as 5.41 Å for crystal planes (002) in the [110] zone axis and 2.71 Å for (020) in the [201] zone axis.
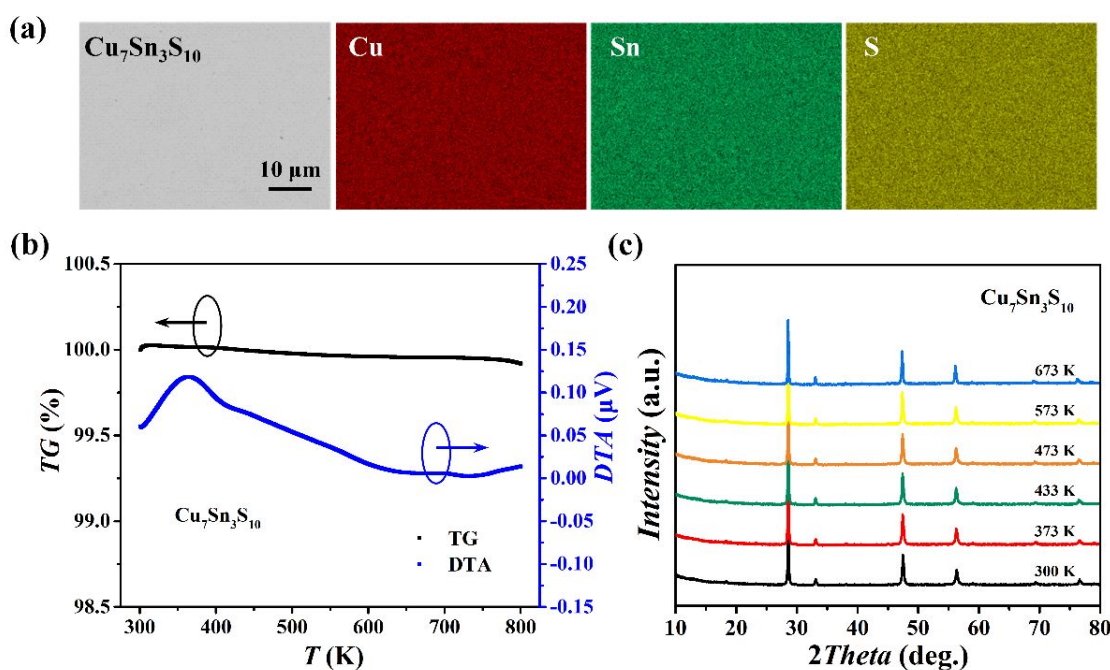

Fig. 3 Characterization of the $Cu_7Sn_3S_{10}$ material prepared by melting-annealing-ball milling method: (a) BSE image and element mapping; (b) Thermal behavior (DTA/TG) between 300 K and 800 K; (c) High-temperature powder XRD (Cu $K\alpha$ radiation, λ = 1.54056 Å).

Table 1. Atomic coordinates and isotropic displacement parameters for $Cu_7Sn_3S_{10}$ (model 2).

Atom	Site	x/a	y/b	z/c	B_{eq} [Å²]	Occupancy
Cu1	2a	0	0	0	0.260	1 Cu
M1	2b	½	½	0	1.160	0.18 Cu+0.82 Sn
M2	4d	0	½	¼	1.130	0.82 Cu+0.18 Sn
S	8i	0.23980	0.23982	0.13060	0.5	1 S

Table 2. Crystallographic information of $Cu_7Sn_3S_{10}$ prepared by melting-annealing-ball milling method (model 2). Here the composition is normalized to 16 atoms in the unit cell.

Composition	$Cu_{5.64}Sn_{2.36}S_{8.00}$
Formula weight	895.075
Space group	$I\bar{4}2m$ (No. 121)
a /Å	5.4164(3)
c /Å	10.832(1)
Unit cell volume /Å³	317.79(7)
F (000) /e	409.6
Z	1
μ/cm⁻¹	593.22
Calculated density (g cm⁻³)	4.65
Radiation, wavelength(Å)	$CuK\alpha$, 1.54056
T (K)	295
Data range 2ϑ (°)	10 - 110
No. of reflections	152
No. of refined structure parameters	7
Profile function	Pseudo-Voigt
Refinement mode	Full profile
R_i	0.0408
R_p	0.0730
R_{wp}	0.0499
Goodness of fit	1.880

The occupational disorder at M1 and M2 sites (Table 1) should lead to strong point defect scattering and thus low lattice thermal conductivity (κ_L). The inset in Fig. 5a plots the total thermal conductivity (κ) for $Cu_7Sn_3S_{10}$. The κ is around 4 W m⁻¹ K⁻¹ at 300 K. It is monotonously decreased to 1.8 W m⁻¹ K⁻¹ at 750 K. The κ_L can be estimated by the expression $\kappa_L = \kappa - L\sigma T$, where L is the Lorenz number calculated by the single parabolic model, which is discussed on more detail later.[41, 42] The calculated κ_L values for $Cu_7Sn_3S_{10}$ are plotted in Fig. 5a. For comparison, the κ_L values for some other typical diamond-like compounds with tetragonal structure are also plotted in Fig. 5a. The κ_L for $Cu_7Sn_3S_{10}$ is about 1.6 W m⁻¹ K⁻¹ at 300 K (Fig. 5a). It decreases with increasing temperature, reaching about 0.24 W m⁻¹ K⁻¹ at 750 K, which is comparable with that of wood. These κ_L values are much lower than those of other reported diamond-like compounds (Fig. 5a) with similar composition and similar to diamond-like compounds with soft, heavy atoms like Hg[43].
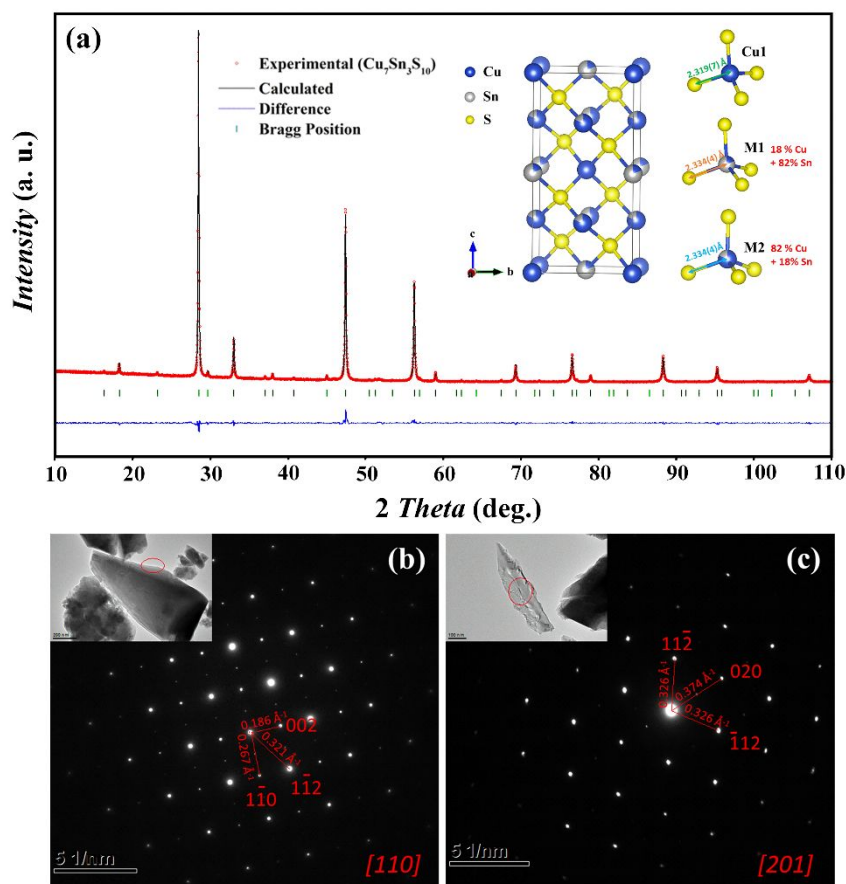
Fig. 4 Crystal structure of $Cu_7Sn_3S_{10}$: (a) total powder X-ray diffraction profile. The red circles represent the measured point intensities. The black lines represent the intensities calculated from the tetragonal structural model (model 2). The blue rough lines show the difference between experimental and calculated intensities. Green vertical bars indicate Bragg positions. The inset shows the final model of tetragonal crystal structure of $Cu_7Sn_3S_{10}$ and three kinds of tetrahedrons wherein. (b-c) Selected area electron diffraction (SAED) performed on $Cu_7Sn_3S_{10}$ particles.

The strong occupational disorder is one of the dominate reasons for the low κ_L of $Cu_7Sn_3S_{10}$ because the disorderedly distributed atoms can introduce strong point defects to scatter phonons. In addition, it is found that the thermal transports of $Cu_7Sn_3S_{10}$ are also influenced by the low-energy localized vibrational states. Here, we measured the low-temperature C_p of $Cu_7Sn_3S_{10}$ and then fit the C_p data by using the equation[44, 45]:

$$\frac{C_p}{T} = \varphi + \beta x + A\Theta_E^2 x^{-3/2} \frac{e^{\frac{\Theta_E}{\sqrt{x}}}}{\left(e^{\frac{\Theta_E}{\sqrt{x}}} - 1 \right)^2} \tag{1}$$

where x represents T^2, φ is the electronic contribution to the heat capacity, β is the Debye contribution from Debye term. The last term in *Eq.* 1 represents the contribution form localized vibrational states, which is also called the Einstein mode. Θ_E is the Einstein temperature of the Einstein mode, and A is a constant. If Einstein mode is not considered, *Eq.* 1 can not give a good fitting for the experimental C_p. This can be confirmed by the results shown in Fig. S1. The fitting curves without using Einstein mode obviously deviate off the experimental data, especially for the C_p/T^3 verse T curve (Fig. S1d). However, if one Einstein mode is considered, *Eq.* 1 can well fit the experimental C_p (Fig. S1), even for the C_p/T^3 verse T curve. The fitting

parameters are given in Table S4. The fitted Θ_E value, 83.1 K, is obtained, corresponding to the presence of one Einstein mode with frequency about 1.7 THz. Fig. 5b demonstrates that this low-energy Einstein mode has a remarkable contribution to the total C_p. Furthermore, the presence of this Einstein mode is confirmed by the calculated phonon dispersion relations. As shown in Fig. S2, low-lying flat optical phonon modes located in the very low-frequency range are observed. In the phonon density of states (PDOS), a peak appears around 2 THz, which is comparable with the Einstein mode derived by the heat capacity fitting.

Generally, the Einstein modes at low-energy range can impede the normal transports of acoustic phonons with similar frequencies and lower lattice thermal conductivity[46, 47]. Fig. 5c shows the measured κ_L below 300 K and the fitting curves based on the Debye-Callaway model[45, 48, 49]:

$$\kappa_L = \frac{k_B}{2\pi^2 v_{avg}} \left(\frac{k_B T}{\hbar} \right)^3 \int_0^{\Theta_D/T} \tau_C \frac{x^4 e^x}{(e^x - 1)^2} dx \tag{2}$$

where $x = \hbar\omega/k_B T$ is the reduced phonon energy, ω is the phonon frequency, $\hbar$ is the reduced Planck constant, k_B is the Boltzmann constant, v_{avg} is the average acoustic velocity (2588 m s^{-1} for $Cu_7Sn_3S_{10}$), and Θ_D is the Debye temperature (285 K for $Cu_7Sn_3S_{10}$). τ_C is the relaxation time, which can be expressed as:
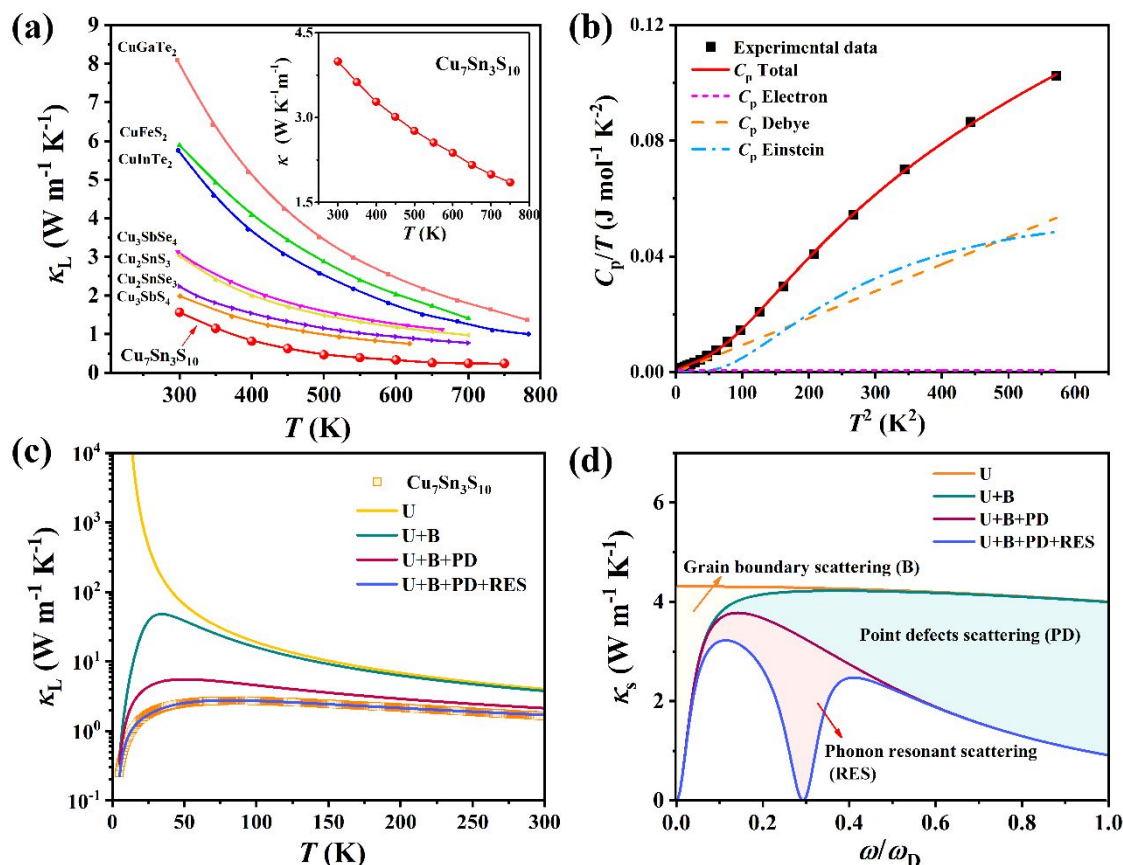
Fig. 5 (a) Lattice thermal conductivity (κ_L) of Cu$_7$Sn$_3$S$_{10}$ (prepared by melting-annealing-ball milling method) from 300 K to 750 K. The κ_L values for some other typical diamond-like compounds with tetragonal structure are also included for comparison (CuGaTe$_2$[50], CuInTe$_2$[50], CuFeS$_2$[51], Cu$_3$SbSe$_4$[52], Cu$_3$SbS$_4$[53], Cu$_2$SnSe$_3$[54], Cu$_2$SnS$_3$[26]). The inset plots the total thermal conductivity (κ) of Cu$_7$Sn$_3$S$_{10}$. (b) C_p/T versus T^2 for Cu$_7$Sn$_3$S$_{10}$ (black squires). The red solid line represents the fitted curve by using one Debye mode and one Einstein mode. The other dashed lines represent the electronic term, Debye term, and Einstein term, respectively. (c) Contributions from various phonon scattering mechanisms to the κ_L of Cu$_7$Sn$_3$S$_{10}$. U, B, PD, and RES denote the phonon-phonon Umklapp process scattering, grain boundary scattering, point defect scattering, and phonon resonant scattering, respectively. (d) Calculated spectral lattice thermal conductivities (κ_s) for Cu$_7$Sn$_3$S$_{10}$ at 300 K.

$$\tau_C^{-1} = \frac{v_{avg}}{L} + A\omega^4 + B\omega^2 Te^{-\Theta_D/3T} + \sum \frac{C_i\omega^2}{\left(\omega_i^2 - \omega^2\right)^2}$$

(3)

The first three terms on the right of *Eq. 3* represent grain-boundary scattering (B), point-defect scattering (PD)[55], and Umklapp process (U). The last term on the right of *Eq. 3* represents the resonant scattering (RES) by low-energy Einstein modes. The resonant frequency derived from the C_p analysis is used for the fitting. As shown in Fig. 5c, the final fitted κ_L curve (blue solid curve) is well consistent with the experimental data (square symbols). The fitting parameters are given in Table S5. The fitted resonant scattering constant (*C*) value is 4.5×10^{36} s^{-3}, which is comparable with those in other typical TE materials with low-frequency Einstein modes, such as Cu$_2$Se[45] and Cu$_8$GeSe$_6$[56]. Then, the contribution of each terms listed in *Eq. 3* can be given. The effect of grain boundary scattering on κ_L reduction mainly works below 50 K. In contrast, the effect of point defect scattering on κ_L reduction is more obvious and it works in the entire temperature range. This is reasonable

because the intrinsic Cu/Sn disorder at the M1 and M2 sites can generate great mass field and strain field fluctuations to interrupt the normal transport of phonons. In addition, the resonant scattering yielded by the low-energy Einstein mode would interact with the acoustic phonons that have similar frequencies to further reduce the κ_L. Thus, the thermal transports of Cu$_7$Sn$_3$S$_{10}$ might be also interpreted by the two-channel conducting mechanism proposed by Mukhopadhyay et al..[57] The role of different phonon scattering mechanisms can be more clearly reflected by Fig. 5d, which shows the spectral lattice thermal conductivities (κ_s) for Cu$_7$Sn$_3$S$_{10}$ at 300 K calculated by[58]

$$\kappa_S(x) = \frac{k_B}{2\pi^2 v_{avg}} \left(\frac{k_B T}{h}\right)^3 \frac{x^4 e^x}{\tau^{-1}(e^x - 1)^2}$$

(4)

In addition, after the phase transformation around 350 K (Fig. 3b), the interstitial copper or even mobile Cu would create additional influence on the phonon transports.[55] To sum up, the

combining effect of these different phonon scattering mechanisms leads to the low κ_L for $Cu_7Sn_3S_{10}$ shown in Fig. 5a.

Beyond the low κ_L, a good TE material also requires moderate band gap for suitable electronic transport. As shown in the inset of Fig. 6a, the band gap for $Cu_7Sn_3S_{10}$ determined by the optical diffuse reflectance spectrum is about 0.64 eV. Fig. 6a-c shows the measured electrical conductivity (σ) and Seebeck coefficient (S) for $Cu_7Sn_3S_{10}$. The σ for $Cu_7Sn_3S_{10}$ is 3.5 ×10^5 S m^{-1} at 300 K. It gradually decreases with increasing temperature, showing metal-like behavior. Likewise, the S increases with increasing temperature, with a maximum value of 106 μV K^{-1} at 750 K (Fig. 6b). The power factors ($PF = S^2\sigma$), which is a comprehensive parameter to evaluate the electrical performance of TE materials, is calculated for $Cu_7Sn_3S_{10}$ with a peak value of 12.8 μW cm^{-1} K^{-2} at 700 K (Fig. 6c). Based on the measured S, σ, and

κ, the dimensionless figure of merit ($zT = S^2\sigma T/\kappa$) is calculated and shown in Fig. 6e. It has a peak zT value of 0.5 at 750 K.

The S for $Cu_7Sn_3S_{10}$ is relatively low as compared with the value typically found at the highest zT in optimally doped materials, around 200 μV K^{-1}.[59, 60] This is caused by its intrinsic high hole concentration (p_H), about 2.7×10^{21} cm^{-3} at 300 K. Here, we doped Cl at the S-sites of $Cu_7Sn_3S_{10}$ with the purpose of reducing the p_H and increase S and zT. The X-ray diffraction patterns of Cl-doped samples are shown in Fig. S3. Interestingly, the diffraction peaks at 18.24°, 23.14°, and 29.72°, which are the typical peaks for the tetragonal structure, disappear upon doping Cl at S-site. The patterns of Cl-doped samples look more like that of cubic structure with space group of $F\bar{4}3m$. This suggests that doping Cl in $Cu_7Sn_3S_{10}$ might induce the structure conversion from tetragonal structure to cubic structure.

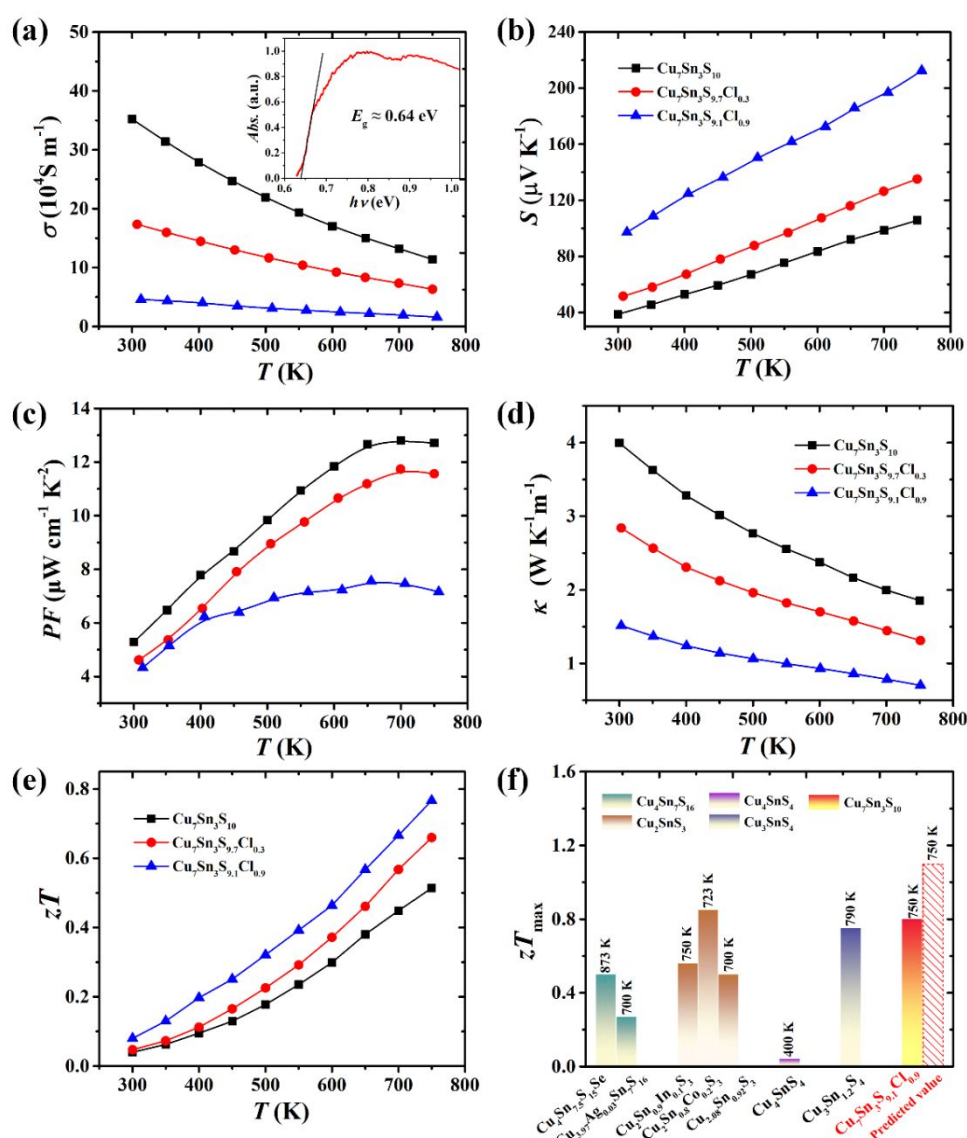**Fig. 6** Temperature dependences of (a) electrical conductivity (σ), (b) Seebeck coefficient (S), (c) power factor (PF), (d) thermal conductivity (κ), and (e) dimensionless figure of merit (zT) for $Cu_7Sn_3S_{10}$, $Cu_7Sn_3S_{9.7}Cl_{0.3}$ and $Cu_7Sn_3S_{9.1}Cl_{0.9}$ samples from 300 K to 750 K. The inset in (a) is the absorption coefficient as a function of photon energy for $Cu_7Sn_3S_{10}$ powders at room temperature. (f) Comparison of zTs for $Cu_7Sn_3S_{10}$ in this work and other typical CTS ternary compounds reported before ($Cu_4Sn_{7.5}S_{15}Se$[30], $Cu_{3.97}Ag_{0.03}Sn_7S_{16}$[31], $Cu_2Sn_{0.9}In_{0.1}S_3$[61], $Cu_2Sn_{0.8}Co_{0.2}S_3$[27], $Cu_{2.08}Sn_{0.92}S_3$[26], Cu_4SnS_4[29], $Cu_3Sn_{1.2}S_4$[28]). The predicted maximum zT for $Cu_7Sn_3S_{10}$ at 750 K based on the effective mass model is also included.

Because Cl has one more valence electron than S, the Cl doped $Cu_7Sn_3S_{10}$, with the chemical composition of $Cu_7Sn_3S_{9.1}Cl_{0.9}$, shows a reduced p_H to 1.2×10^{21} cm^{-3} at 300 K. Correspondingly, the S for $Cu_7Sn_3S_{9.1}Cl_{0.9}$ is enhanced in the entire measured temperature range. At 300 K, the S for $Cu_7Sn_3S_{9.1}Cl_{0.9}$ is 97 μV K^{-1}, about a 150% enhancement as compared with the pristine $Cu_7Sn_3S_{10}$ (Fig. 6b). However, the S enhancement is not enough to compensate the σ reduction, thus the PFs for the Cl-doped samples are lower than that of the pristine $Cu_7Sn_3S_{10}$ (Fig. 6c). Likewise, the suppressed carrier thermal conductivity (Fig. S4) due to the σ reduction leads to the significant κ reduction (Fig. 6d). The κ for $Cu_7Sn_3S_{9.1}Cl_{0.9}$ is 1.5 W m^{-1} K^{-1} at 300 K, about 62% reduction as compared with the pristine $Cu_7Sn_3S_{10}$. Finally, due to the enhanced S and reduced κ, $Cu_7Sn_3S_{9.1}Cl_{0.9}$ shows greatly enhanced zT throughout the entire range of measured temperatures. At 750 K, a maximum zT of 0.8 is achieved for $Cu_7Sn_3S_{9.1}Cl_{0.9}$ (Fig. 6e). As show in Fig. 6f, this value is among the highest values reported in CTS ternary compounds. If κ can be further suppressed, even higher values of zT can be expected. By combining elements that are low cost, nontoxic, and earth-abundant, $Cu_7Sn_3S_{10}$ shows great potential to be used in the waste heat recovery industry.

In order to predict how zT can be further enhanced, an analysis of the doping efficiency and effective material parameters was performed for the $Cu_7Sn_3S_{10-x}Cl_x$ system using an effective mass model (EMM)[60, 62], which gives the effective carrier effective mass and mobility based on the experimental measurements. Often the effective mass model is called the single parabolic band model (SPB) although no assumption of single or parabolic bands (or scattering assumption) is required to do the analysis. According to the measured X-ray photoelectron spectroscopy for $Cu_7Sn_3S_{10}$ (Fig. S5), the valence states of Cu, Sn, and S can be determined to be +1, +4, and -2, respectively.[26, 39] The hole concentration found in $Cu_7Sn_3S_{10}$ is consistent with that expected from valence counting. The substitution of a Cl$^-$ for S^{2-} decreases the hole concentration (Fig. 7a), but the decrease in Hall carrier concentration is about 50% less than that expected based on the assumption that the introduction of one Cl ion removes one hole. This lower doping efficiency can be explained by the formation of compensating defects, such as negatively in charged Cu vacancies. For each Cu vacancy that is formed, an additional hole is formed, explaining the higher than expected Hall carrier concentration. Similar behavior has been observed in $Cu_{2-y}Se_{1-x}Br_x$.[63] In this system, the substitution of Br for Se is expected to removed one hole, but also exhibits a doping efficiency of 50%.[63]

In the effective mass model, the valence band is characterized by a density of states effective mass m_d^*, which can be extracted from Hall effect and Seebeck coefficient data. The effective mass model can also be used to find the TE quality factor, B, which provides a description for the maximum zT that can be achieved in a material given the optimal carrier concentration.[60] The quality factor B is given in Eq. 5, where μ_0 is the mobility

parameter. The electronic contribution to B is characterized by weighted mobility μ_w (Eq. 6)[42, 62]

$$B = \frac{\mu_0 \left(\dfrac{m_d^*}{m_e}\right)^{3/2} T^{5/2}}{\kappa_L} \quad (5)$$

$$\mu_w = \mu_0 \left(\frac{m_d^*}{m_e}\right)^{3/2} \quad (6)$$

The effective mass model was used to analyze and predict the TE performance of $Cu_7Sn_3S_{10-x}Cl_x$ based on room temperature Hall effect measurements. The Pisarenko relationship (Fig. 7b) between the Seebeck coefficient and the carrier concentration was used to approximate the m_d^*. Each sample requires a different m_d^* to accurately model this relationship, and the effective mass appears to increase with increasing Cl content. Likewise, doping Cl would introduce additional alloying scattering or ionized impurity scattering to the charged carriers, which can be confirmed by the scenario shown in Fig. S6 that the temperature dependence of Hall mobility significantly deviates off $T^{-1.5}$ rule for the Cl-doped samples. The increase of effective mass, as well as the additional scattering to charge carriers, would result in the decreased Hall mobility with decreasing Hall carrier concentration (i.e. increasing Cl-doping content), which is consistent with the result shown in Fig. 7c.[64, 65] In this case, the three $Cu_7Sn_3S_{10-x}Cl_x$ samples should have different μ_0 values. Thus, here the μ_0 and m_d^* values used to predict zT are taken as the median values of the three compositions (i.e. the values for x=0.3). The κ_L is chosen as 1.7 W m^{-1} K^{-1}. These parameters yield a B value of 0.04 and a good modelling of experimental measured zT as a function of carrier concentration at room temperature for all three $Cu_7Sn_3S_{10-x}Cl_x$ samples (Fig. 7d). It can be seen that at room temperature zT can be optimized by decreasing the carrier concentration, or increasing the Cl content.

Using the parameters determined at room temperature, the weighted mobility μ_w, lattice thermal conductivity κ_L, and TE quality factor B were calculated at higher temperatures, and used to predict the maximum attainable zT at these temperatures. Fig. S7a shows that the κ_L values for $Cu_7Sn_3S_{10}$ are comparable with those for the Cl-doped samples around room temperature, but much lower than those at high temperatures. This might be related with the tetragonal-cubic structure conversion and the disappearance of the distorted non-cubic framework due to the Cl-doping mentioned above. Furthermore, in Fig. S7b, it can be seen that the weighted mobility μ_w decreases with increasing temperature and Cl-doping content. The rate of decrease is lower for compositions with higher Cl content, which suggests that the mobility is less sensitive to temperature when x increases and carrier concentration decreases. This change in temperature dependence could be explained by an increase in alloy scattering or ionized impurity scattering strength upon the addition of Cl, which is consistent with the result shown in Fig. S6.
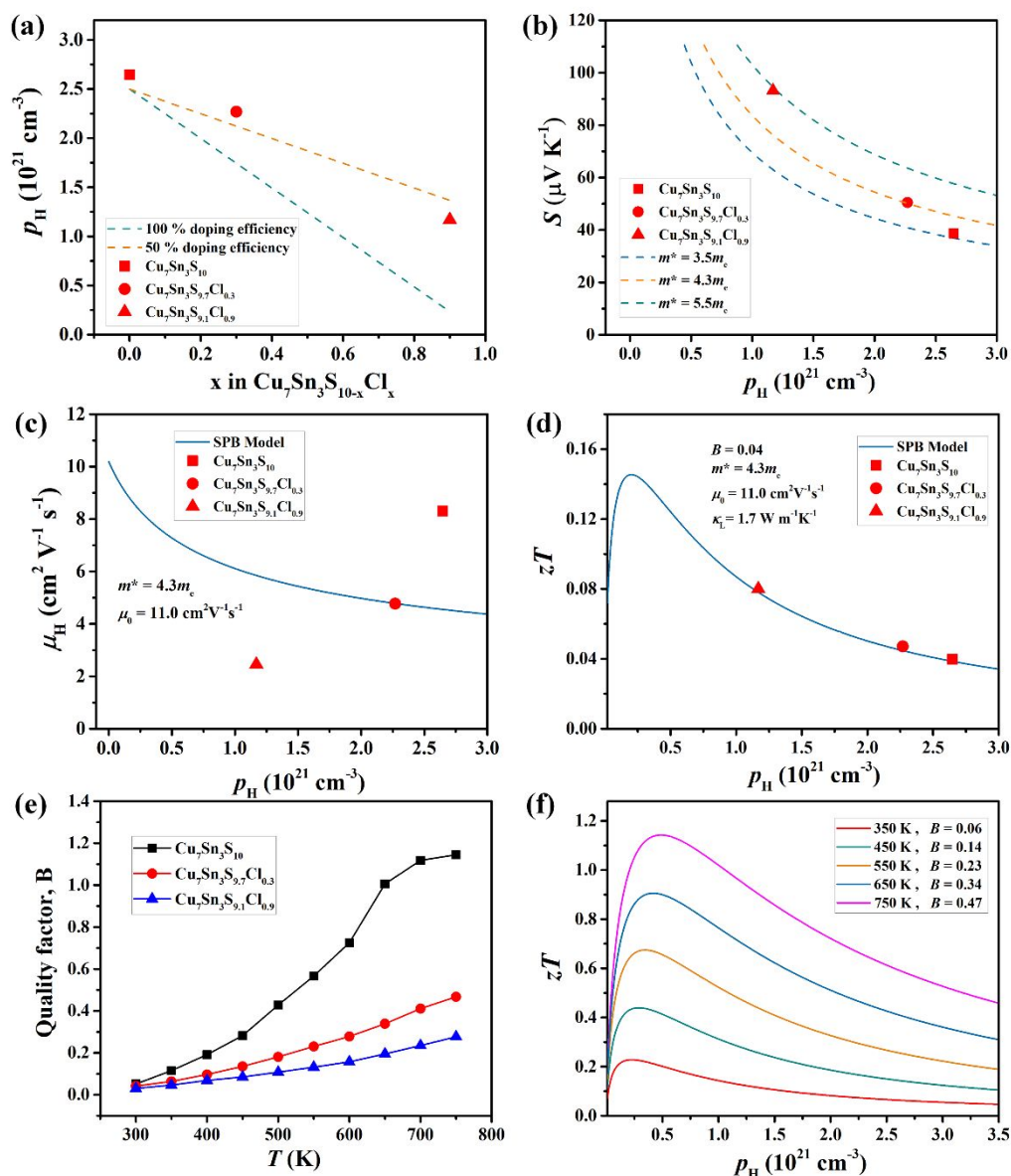
Fig. 7 Electrical transport properties of in $Cu_7Sn_3S_{10-x}Cl_x$ at 300 K and comparison with an effective mass model. (a) Doping efficiency of Cl in $Cu_7Sn_3S_{10-x}Cl_x$. The measured Hall carrier concentration p_H matches that expected from the valence electron count of $Cu_7Sn_3S_{10}$. The addition of Cl removes holes as expected but at about 50% efficiency suggesting the existence of compensating defects. (b) Pisarenko relationship for the Seebeck coefficient vs. Hall carrier concentration giving density-of-state effective mass m_d^*. (c) Hall mobility μ_H vs. carrier concentration for $Cu_7Sn_3S_{10-x}Cl_x$. The lines in b and c represent the theoretical curves predicted by the single parabolic model assuming that acoustic phonon scattering is dominated. (d) Prediction of zT vs. carrier concentration derived from room temperature estimates of the quality factor B, mobility parameter μ_0, lattice thermal conductivity κ_L, and effective mass m_d^*. (e) Calculated TE quality factor B for $Cu_7Sn_3S_{10-x}Cl_x$. (f) Predicted zT as a function of carrier concentration based on the effective mass model. A maximum zT of 1.1 is predicted for a carrier concentration of about 5×10^{20} cm^{-3} at 750 K.

Fig. 7e presents the B values for $Cu_7Sn_3S_{10-x}Cl_x$ samples. Although the B for $Cu_7Sn_3S_{10}$ is significantly higher than those for the Cl-doped samples, especially at high temperature, due to high μ_w and low κ_L (Fig. S7), it does not exhibit the highest zT because its hole concentration deviates the most from the optimal carrier concentration at each temperature (Fig. 7d). The B value at each temperature used to predict zT was taken as the median value of the three compositions at that temperature

(i.e. the value for x=0.3). Based on this analysis, Fig. 7f shows that a relatively high maximum zT of 1.1 is achievable at 750 K for a carrier concentration of about 5×10^{20} cm^{-3}, which is lower than the minimum Hall carrier concentration that was measured at room temperature of 1.2×10^{21} cm^{-3}. This prediction explains why the sample with x= 0.9 has the highest zT despite having the lowest B, i.e. it has the lowest hole concentration and therefore the carrier concentration closest

to the optimal value. Being limited by the low Cl-doping content in $Cu_7Sn_3S_{10}$ (Fig. S3), higher zT can be expected if the *n*-type dopant has a higher doping limit or efficiency than Cl, but the dopability may be limited by intrinsic defects[66].

Conclusions

In summary, the modified diffusion-couple HTP synthesis method and automated histogram analysis technique have been developed to quickly screen the new CTS compounds. Ternary $Cu_7Sn_3S_{10}$ compound has been successfully discovered and fabricated. The characterizations on the crystal structure, optical band gap, electrical and thermal transport properties, prove that $Cu_7Sn_3S_{10}$ is a promising TE material. Via doping Cl into $Cu_7Sn_3S_{10}$, a peak zT of 0.8 at 750 K has been achieved, among the highest values reported in CTS compounds. Based on the effective mass model, an even higher zT of 1.1 is attainable at 750 K by further decreasing the carrier concentration. This study shows that the modified diffusion-couple HTP synthesis method and automated histogram analysis technique may provide a powerful strategy to develop various new functional materials.

Experimental section

High-throughput synthesis: The pre-synthesized CuS and SnS powders were mixed in agate mortar by hands with nine different mole ratios, termed 10:90, 20:80, 30:70, 40:50, 50:50, 60:40, 70:30, 80:20, and 90:10. These mixtures were loaded into the graphite die with a diameter of 10 mm in sequence. After loading each mixture into the graphite die, a pressure of 5 MPa was stressed on the powders to flatten the surface. After all the mixtures were loaded, they were sintered at the isothermal temperature of 700 K for 15 min under the pressure of 60 MPa by Spark Plasma Sintering (Sumitomo, SPS-2040). The sintered nine-segment bulk sample were annealed at 700 K for 3 days to promote the reaction between CuS and SnS forming CTS compounds. Then, a piece was cut from the nine-segment bulk in the direction parallel to the sintering press. This piece was polished to characterize the microstructure and chemical composition by Scanning electron microscopy (SEM, ZEISS supra 55, Germany). We adopted the nine-segment sample instead of directly sintering one CuS layer and one SnS layer together into a two-segment sample because the limited element diffusion and slow reaction at the interface of the segments will yield very low reaction rate.

Synthesis of $Cu_7Sn_3S_{10}$–based materials: $Cu_7Sn_3S_{10-x}Cl_x$ (x = 0, 0.3 and 0.9) samples were synthesized by the melting-annealing-ball milling method. High-purity raw materials of Cu (shots, 99.999%, Alfa Aesar), Sn (shots, 99.999%, Alfa Aesar), S (pieces, 99.999%, Alfa Aesar), and CuCl (powder, 99.9%, Alfa Aesar) were weighed out based on the chemical ratio as designed, and then sealed in quartz tubes under vacuum. The sealed quartz tube was put into the furnace and heated to 723 K in 4.5 hours, held at this temperature for 2 hours, and then further heated to 1223 K in 5 hours and kept at this temperature

for 3.5 hours. After that, the temperature was decreased to 1073 K in 3 hours and kept at this temperature for 2 days. Finally, the tube was slowly cooled to room temperature in 16 hours. The ingot was then balled milled in a WC jar at a speed of 500 rpm for 5 hours in the Argon atmosphere. The obtained powder was sintered at 923 K under a uniaxial pressure of 65 MPa for 10 minutes by Spark Plasma Sintering. The sintering was conducted in argon atmosphere with a low pressure of about 0.07 MPa.

Characterization: The chemical components were characterized by Scanning electron microscopy (SEM, ZEISS supra 55, Germany) with Energy Dispersive X-ray Spectroscopy (EDS, Oxford, UK). The X-ray powder diffraction pattern of $Cu_7Sn_3S_{10}$ sample was carried out using LaB_6 as internal standard (a = 4.157 Å) and analyzed by the least-squares refinement method employing the WinCSD program package.[67] The final refinement involved the following parameters: zero shift, scale factor, asymmetry parameter, peak half-width parameters, unit cell parameters, positional parameters and isotropic temperature factors. Transmission electron microscopy (TEM, JEM-1400, Japan) with selected area electron diffraction (SAED) were used to confirm the crystal structure. The optical band gap was calculated from the intercepts of the plots of A versus photon energy $h\upsilon$ based on the equation of $A = B (h\upsilon - E_g)^{68}$, where A is the absorption coefficient, $h\upsilon$ is the incident photon energy, and B is the band tailing parameter. The optical absorption coefficient (A) was conducted on powder samples by using the UV-Vis spectrum (Shimadzu Spectroscope, UV-3101PC, Japan) at room temperature. The electrical conductivity (σ) and Seebeck coefficient (S) were measured from 300 K to 750 K by using ZEM-3 (Ulvac-Riko Japan). The thermal conductivity (κ) was calculated by the formula $\kappa = \rho C_p \lambda$, where ρ is the density measured based on the Archimedes principle, C_p is the heat capacity estimated via the Dulong-Petit law, and λ is thermal diffusivity measured by using the Laser flash method (LFA457, Netzsch, Germany). The thermal conductivity and heat capacity in low temperature range (2-300 K) were measured by Physical Property Measurement System (PPMS, Quantum Design, USA). The velocity of sound (v) was measured by using the Advanced Ultrasonic measurement system (UMS, TECLAB, France).

Author contributions

P. Q. and X. S. designed the experiments. T. D. performed material syntheses and sample measurements. T. X., I. V. and Y. G. analyzed the crystal structure of the new compound ($Cu_7Sn_3S_{10}$). Y. S. and J. Y. analyzed the modified diffusion-couple by automated histogram analysis technique. M. B. analyzed the electrical transport properties by an effective mass model (EMM). T. D. and P. Q. wrote the manuscripts. Q. S., T-R. W., X. S., J. Y., Y. G., L. C. and G. J. revised the manuscripts. All authors discussed the results and commented on the manuscript.

Conflicts of interest

There are no conflicts to declare.

Acknowledgements

References

1.   C. Ward, *Materials Genome Initiative for Global Competitiveness*, USA, 2012.
2.   A. Jain, S. P. Ong, G. Hautier, W. Chen, W. D. Richards, S. Dacek, S. Cholia, D. Gunter, D. Skinner, G. Ceder and K. A. Persson, *APL Mater.* , 2013, **1**, 011002.
3.   J. Carrete, W. Li, N. Mingo, S. Wang and S. Curtarolo, *Phys. Rev. X*, 2014, **4**, 011019
4.   M. Liu, Z. Rong, R. Malik, P. Canepa, A. Jain, G. Ceder and K. A. Persson, *Energy Environ. Sci.*, 2015, **8**, 964-974.
5.   L. L. Xi, S. S. Pan, X. Li, Y. L. Xu, J. Y. Ni, X. Sun, J. Yang, J. Luo, J. Y. Xi, W. H. Zhu, X. R. Li, D. Jiang, R. Dronskowski, X. Shi, G. J. Snyder and W. Q. Zhang, *J Am. Chem. Soc.*, 2018, **140**, 10785-10793.
6.   S. Bang, J. Kim, D. Wee, G. Samsonidze and B. Kozinsky, *Mater. Today Phys.*, 2018, **6**, 22-30.
7.   Y. W. Lai, S. Hamann, M. Ehmann and A. Ludwig, *Rev. Sci. Instrum.*, 2011, **82**, 063903.
8.   C. Khare, K. Sliozberg, A. Stepanovich, W. Schuhmann and A. Ludwig, *Nanotechnology*, 2017, **28**, 185604.
9.   J. R. O'Dea, M. E. Holtz, A. E. Legard, S. D. Young, R. G. Burns, A. R. Van Wassen, D. A. Muller, H. D. Abruña, F. J. DiSalvo, R. B. van Dover and J. A. Marohn, *Chem. Mater.* , 2015, **27**, 4515-4524.
10.   A. J. Urquhart, D. G. Anderson, M. Taylor, M. R. Alexander, R. Langer and M. C. Davies, *Adv. Mater.*, 2007, **19**, 2486-2491.
11.   Y. Zhao and C. Burda, *Energy Environ. Sci.*, 2012, **5**, 5564-5576.
12.   K. Ramasamy, R. K. Gupta, S. Palchoudhury, S. Ivanov and A. Gupta, *Chem. Mater.* , 2014, **27**, 379-386.
13.   T. Wada, S. Nakamura and T. Maeda, *Prog. Photovolt: Res. Appl.*, 2012, **20**, 520-525.
14.   F. W. d. S. Lucas and A. Zakutayev, *APL Mater.* , 2018, **6**, 084501.
15.   A. C. Lokhande, P. T. Babar, V. C. Karade, M. G. Gang, V. C. Lokhande, C. D. Lokhande and J. H. Kim, *J. Mater. Chem. A*, 2019, **7**, 17118-17182.
16.   P. Qiu, X. Shi and L. Chen, *Energy Storage Mater.*, 2016, **3**, 85-97.
17.   T.-R. Wei, Y. Qin, T. Deng, Q. Song, B. Jiang, R. Liu, P. Qiu, X. Shi and L. Chen, *Sci. China Mater.*, 2018, **62**, 8-24.
18.   X. Shi and L. Chen, *Nat. Mater.*, 2016, **15**, 691-692.
19.   J. He and T. M. Tritt, *Science*, 2017, **357**.
20.   W. Liu, J. Hu, S. Zhang, M. Deng, C.-G. Han and Y. Liu, *Mater. Today Phys.*, 2017, **1**, 50-60.
21.   C. Uher, *Materials Aspect of Thermoelectricity*, CRC Press, Boca Raton, 2017.
22.   R. Nunna, P. Qiu, M. Yin, H. Chen, R. Hanus, Q. Song, T. Zhang, M.-Y. Chou, M. T. Agne, J. He, G. J. Snyder, X. Shi and L. Chen, *Energy Environ. Sci.*, 2017, **10**, 1928-1935.
23.   K. Zhao, C. Zhu, P. Qiu, A. B. Blichfeld, E. Eikeland, D. Ren, B. B. Iversen, F. Xu, X. Shi and L. Chen, *Nano Energy*, 2017, **42**, 43-50.
24.   X. Lu, D. T. Morelli, Y. Xia and V. Ozolins, *Chem. Mater.* , 2015, **27**, 408-413.
25.   X. Wang, P. Qiu, T. Zhang, D. Ren, L. Wu, X. Shi, J. Yang and L. Chen, *J. Mater. Chem. A*, 2015, **3**, 13662-13670.
26.   T. Deng, P. Qiu, Q. Song, H. Chen, T.-R. Wei, L. Xi, X. Shi and L. Chen, *J. Appl. Phys.*, 2019, **126**, 085111.
27.   H. Zhao, X. Xu, C. Li, R. Tian, R. Zhang, R. Huang, Y. Lyu, D. Li, X. Hu, L. Pan and Y. Wang, *J. Mater. Chem. A*, 2017, **5**, 23267-23275.
28.   Y. B. Yang, P. Z. Ying, J. Z. Wang, X. L. Liu, Z. L. Du, Y. M. Chao and J. L. Cui, *J. Mater. Chem. A*, 2017, **5**, 18808-18815.
29.   A. Choudhury, S. Mohapatra, H. Yaghoobnejad Asl, S. H. Lee, Y. S. Hor, J. E. Medvedeva, D. L. McClane, G. E. Hilmas, M. A. McGuire, A. F. May, H. Wang, S. Dash, A. Welton, P. Boolchand, K. P. Devlin, J. Aitken, R. Herbst-Irmer and V. Petříček, *J. Solid State Chem.*, 2017, **253**, 192-201.
30.   J. Cui, J. He, Z. Han, X. Liu and Z. Du, *Sci. Rep.*, 2018, **8**, 8202.
31.   T. Deng, T.-R. Wei, Q. Song, Q. Xu, D. Ren, P. Qiu, X. Shi and L. Chen, *RSC Adv.*, 2019, **9**, 7826-7832.
32.   S. Fiechter, M. Martinez, G. Schmidt, W. Henrion and Y. Tomm, *J. Phys. Chem. Solids*, 2003, **64**, 1859-1862.
33.   D. Wu, C. R. Knowles and L. L. Y. Chang, *Mineral. Mag.*, 1986, **50**, 323-325.
34.   J. Zhang, Y. Yan, H. Xie, T. Zhu, C. Zhang, J. Qiu, L. Yao and X. Tang, *Ceram. Int.*, 2019, **45**, 16039-16045.
35.   B. Chen, M. Zhou, T. Jiang and L. Li, *J. Alloy. Compd.*, 2019, **802**, 103-111.
36.   N. Otsu, *IEEE Trans. Syst. Man Cybern.*, 1979, **SMC-9**, 62-66.
37.   W. G. Zeier, A. LaLonde, Z. M. Gibbs, C. P. Heinrich, M. Panthofer, G. J. Snyder and W. Tremel, *J. Am. Chem. Soc.*, 2012, **134**, 7147-7154.
38.   W. G. Zeier, C. P. Heinrich, T. Day, C. Panithipongwut, G. Kieslich, G. Brunklaus, G. J. Snyder and W. Tremel, *J. Mater. Chem. A*, 2014, **2**, 1790-1794.
39.   Q. Song, P. Qiu, F. Hao, K. Zhao, T. Zhang, D. Ren, X. Shi and L. Chen, *Adv. Electron. Mater.*, 2016, **2**, 1600312.
40.   C. Wang, S. Chen, J.-H. Yang, L. Lang, H.-J. Xiang, X.-G. Gong, A. Walsh and S.-H. Wei, *Chem. Mater.* , 2014, **26**, 3411-3417.
41.   T. M. Tritt, ed., *Thermal Conductivity Theory, Properties, and Applications*, Kluwer Academic / Plenum Publishers, New York, 2004.
42.   A. F. May and G. J. Snyder, in *Thermoelectrics and its energy harvesting*, ed. D. M. Rowe, CRC Press, Boca Racon, 2012, ch. 11, pp. 1-18.
43.   B. R. Ortiz, W. Peng, L. C. Gomes, P. Gorai, T. Zhu, D. M. Smiadak, G. J. Snyder, V. Stevanović, E. Ertekin, A. Zevalkink and E. S. Toberer, *Chem. Mater.*, 2018, **30**, 3395-3409.
44.   I. K. Dimitrov, M. E. Manley, S. M. Shapiro, J. Yang, W. Zhang, L. D. Chen, Q. Jie, G. Ehlers, A. Podlesnyak, J. Camacho and Q. Li, *Phys. Rev. B*, 2010, **82**, 174301.

45. H. L. Liu, J. Yang, X. Shi, S. A. Danilkin, D. Yu, C. Wang, W. Zhang and L. Chen, *J. Materiomics*, 2016, **2**, 187-195.

46. M. T. Agne, K. Imasato, S. Anand, K. Lee, S. K. Bux, A. Zevalkink, A. J. E. Rettie, D. Y. Chung, M. G. Kanatzidis and G. J. Snyder, *Mater. Today Phys.*, 2018, **6**, 83-88.

47. M. Christensen, A. B. Abrahamsen, N. B. Christensen, F. Juranyi, N. H. Andersen, K. Lefmann, J. Andreasson, C. R. Bahl and B. B. Iversen, *Nat. Mater.*, 2008, **7**, 811-815.

48. J. Callaway, *Phys. Rev.*, 1959, **113**, 1046-1051.

49. J. Callaway and H. C. V. Baeyer, *Phys. Rev.*, 1960, **120**, 1149-1154.

50. Y. T. Qin, P. F. Qiu, R. H. Liu, Y. L. Li, F. Hao, T. S. Zhang, D. D. Ren, X. Shi and L. D. Chen, *J. Mater. Chem. A*, 2016, **4**, 1277-1289.

51. Y. Li, T. Zhang, Y. Qin, T. Day, G. J. Snyder, X. Shi and L. Chen, *J. Appl. Phys.*, 2014, **116**, 203705.

52. E. J. Skoug, J. D. Cain and D. T. Morelli, *Appl Phys Lett*, 2011, **98**, 261911.

53. K. Chen, B. Du, N. Bonini, C. Weber, H. Yan and M. J. Reece, *J. Phys. Chem. C* 2016, **120**, 27135-27140.

54. J. Fan, W. Schnelle, I. Antonyshyn, I. Veremchuk, W. Carrillo-Cabrera, X. Shi, Y. Grin and L. Chen, *Dalton T.*, 2014, **43**, 16788-16794.

55. R. Gurunathan, R. Hanus, M. Dylla, A. Katre and G. J. Snyder, *Phys. Rev. Appl.*, 2020, **13**.

56. B. B. Jiang, P. Qiu, E. Eikeland, H. Chen, Q. Song, D. Ren, T. Zhang, J. Yang, B. B. Iversen, X. Shi and L. Chen, *J. Mater. Chem. C*, 2017, **5**, 943-952.

57. S. Mukhopadhyay, D. S. Parker, B. C. Sales, A. A. Puretzky, M. A. McGuire and L. Lindsay, *Science*, 2018, **360**, 1455–1458

58. T. J. Zhu, C. G. Fu, H. H. Xie, Y. T. Liu, B. Feng, J. Xie and X. B. Zhao, *Europhys. Lett.*, 2013, **104**.

59. S. Kang and G. Snyder, 2017, https://arxiv.org/pdf/1710.06896.pdf.

60. A. Zevalkink, D. M. Smiadak, J. L. Blackburn, A. J. Ferguson, M. L. Chabinyc, O. Delaire, J. Wang, K. Kovnir, J. Martin, L. T. Schelhas, T. D. Sparks, S. D. Kang, M. T. Dylla, G. J. Snyder, B. R. Ortiz and E. S. Toberer, *Appl. Phys. Rev.*, 2018, **5**.

61. Q. Tan, W. Sun, Z. Li and J.-F. Li, *J. Alloy. Compd.*, 2016, **672**, 558-563.

62. G. J. Snyder, A. H. Snyder, M. Wood, R. Gurunathan, B. H. Snyder and C. Niu, *Adv. Mater.*, 2020, **32**, e2001537.

63. T. W. Day, K. S. Weldert, W. G. Zeier, B.-R. Chen, S. L. Moffitt, U. Weis, K. P. Jochum, M. Panthöfer, M. J. Bedzyk, G. J. Snyder and W. Tremel, *Chem. Mater.*, 2015, **27**, 7018-7027.

64. J. Bardeen and W. Shockley, *Phys. Rev.*, 1950, **80**, 72-80.

65. J. W. Harrison and J. R. Hauser, *Phys. Rev. B*, 1976, **13**, 5347-5350.

66. S. A. Miller, M. Dylla, S. Anand, K. Gordiz, G. J. Snyder and E. S. Toberer, *npj Comput. Mater.*, 2018, **4**.

67. L. Akselrud and Y. Grin, *J. Appl. Cryst.*, 2014, **47**, 803-805.

68. R. López and R. Gómez, *J. Sol-Gel Sci. Technol*, 2011, **61**, 1-7.

Electronic Supplementary Information

Discovery of high-performance thermoelectric copper chalcogenide using modified diffusion-couple high-throughput synthesis and automated histogram analysis technique

Tingting Deng, [abc] Tong Xing, [ab] Madison Brod, [d] Ye Sheng, [e] Pengfei Qiu,*[ab] Igor Veremchuk, [f] Qingfeng Song, [ab] Tian-Ran Wei, [g] Jiong Yang, [ae] G. Jeffrey Snyder,*[d] Yuri Grin, [h] Lidong Chen [ab] and Xun Shi*[a]

a. State Key Laboratory of High Performance Ceramics and Superfine Microstructure, Shanghai Institute of Ceramics, Chinese Academy of Sciences, Shanghai 200050, China. E-mail: xshi@mail.sic.ac.cn, qiupf@mail.sic.ac.cn
b. Center of Materials Science and Optoelectronics Engineering, University of Chinese Academy of Sciences, Beijing 100049, China.
c. School of Physical Science and Technology, Shanghai Tech University, Shanghai 201210, China.
d. Department of Materials Science and Engineering, Northwestern University, Evanston, Illinois 60208, USA. E-mail: jeff.snyder@northwestern.edu
e. Materials Genome Institute, Shanghai University, Shanghai 200444, China.
f. Helmholtz-Zentrum Dresden-Rossendorf, Institute of Ion Beam Physics and Materials Research, 01328 Dresden, Germany.
g. State Key Laboratory of Metal Matrix Composites, School of Materials Science and Engineering, Shanghai Jiao Tong University, Shanghai 200240, China.
h. Max-Planck-Institut für Chemische Physik fester Stoffe, Dresden, Germany.

Lattice dynamics calculations

Lattice dynamics were obtained by Density-Functional Theory (DFT) calculations with Vienna ab initio simulation package (VASP)[1, 2], using the frozen phonon method which is implemented in the Phonopy package. The projector-augmented wave (PAW) method as implemented in the Perdew−Burke−Ernzerhof (PBE)-type generalized gradient approximation (GGA) was used as the exchange−correlation functional[3]. Based on the crystallographic information obtained by the X-ray refinement (model 2), we firstly built an order $2 \times 2 \times 2$ supercell of Cu_3SnS_4. Then, two Cu atoms in the

supercell are replaced by Sn atoms to form the chemical composition ($Cu_{22}Sn_{10}S_{32}$) that is close to $Cu_7Sn_3S_{10}$ based on special quasirandom structures (SQS's) calculations.[4] The plane-wave energy cutoff was set at 450 eV and a $3\times 3 \times 3$ Monkhorst-Pack k mesh was used for crystal structure optimization to realize the convergence of Hellmann–Feynman forces. It is adopted that convergence criteria of 5×10^{-5} eV/Å for relaxation process of unit cell and 5×10^{-7} eV/Å for static calculation of displaced supercell at gamma point in accurate precision. The spin-orbit coupling (SOC) effect has not been considered.

Table S1 Crystallographic information of $Cu_7Sn_3S_{10}$ prepared by melting-annealing-ball milling method (model 1). Here the composition is normalized to 16 atoms in the unit cell.

Composition	$Cu_{6.28}Sn_{1.72}S_{8.00}$
Formula weight	859.77
Space group	$I\bar{4}2m$ (No. 121)
a /Å	5.4163(3)
c /Å	10.833(1)
Unit cell volume /Å^3	317.79(7)
F (000) /e	396.1
Z	1
μ/cm^{-1}	502.62
Calculated density (g cm^{-3})	4.492(1)
Radiation, wavelength(Å)	Cu$K\alpha$, 1.54056
T (K)	295
Data range 2θ (°)	10 - 110
No. of reflections	152
No. of refined structure parameters	7

Profile function	Pseudo-Voigt
Refinement mode	Full profile
R_i	0.0393
R_p	0.0720
R_{wp}	0.0489
Goodness of fit	1.850

Table S2 Crystallographic information of $Cu_7Sn_3S_{10}$ prepared by melting-annealing-ball milling method (model 3). Here the composition is normalized to 16 atoms in the unit cell.

Composition	$Cu_{5.56(2)}Sn_{2.33(4)}S_{8.10(2)}$
Formula weight	890.3
Space group	$I\bar{4}2m$ (No. 121)
a /Å	5.4162(2)
c /Å	10.8335(7)
Unit cell volume /Å^3	317.80(5)
F (000) /e	407.5
Z	1
μ/cm^{-1}	589.3
Calculated density (g cm^{-3})	4.65
Radiation, wavelength(Å)	Cu $K\alpha$, 1.54056
T (K)	295
Data range 2θ (°)	10 - 110
No. of reflections	152
No. of refined structure parameters	7
Profile function	Pseudo-Voigt
Refinement mode	Full profile
R_i	0.032
R_p	0.050
R_{wp}	0.067
Goodness of fit	1.76

Table S3 Selected Bond Lengths (Å) and Angles (°) for $Cu_7Sn_3S_{10}$ in the model 2.

Cu1-S1	2.319(7)		
Cu2-S1	2.334(4)		
Cu3-S1	2.334(4)		
S1-Cu1-a S1 7)	111.86(2)	a S1-Cu2-b S1 7) [0010]	109.58(2)
S1-Cu1-b S1 7) [0000]	104.78(2)	a S1-Cu2-c S1	109.25(2)
S1-Cu1-c S1 7) [0000]	111.86(2)	b S1-Cu2-c S1	109.58(2)
a S1-Cu1-b S1 7) [0000]	111.86(2)	S1-Cu3-a S1 6)	111.99(2)
a S1-Cu1-c S1	104.78(2)	S1-Cu3-a S1 6) [0010]	108.23(2)
b S1-Cu1-c S1	111.86(2)	S1-Cu3-c S1 6) [0000]	108.23(2)
S1-Cu2-a S1 7)	109.58(2)	a S1-Cu3-b S1 6) [0-100]	108.23(2)
S1-Cu2-b S1 7) [0100]	109.25(2)	a S1-Cu3-c S1	108.23(2)
S1-Cu2-c S1 7) [0110]	109.58(2)	b S1-Cu3-c S1	111.99(2)

Symmetry codes: (1) x, y, z; (2) -y, x, -z; (3) -x, -y, z; (4) y, -x, -z; (5) -x, y, -z; (6) y, x, z; (7) x, -y, -z; (8) -y, -x, z; (9) 1/2+x, 1/2+y, 1/2+z ; (10) 1/2-y , 1/2+x , 1/2-z ; (11) 1/2-x, 1/2-y, 1/2+z ; (12) 1/2+y , 1/2-x , 1/2-z ; (13) 1/2-x, 1/2+y, 1/2-z ; (14) 1/2+y, 1/2+x, 1/2+z ; (15) 1/2+x , 1/2-y , 1/2-z ; (16) 1/2-y , 1/2-x, 1/2+z.

Table S4 Parameters used to fit the heat capacity (C_p) data of $Cu_7Sn_3S_{10}$ by using a Debye and two Einstein modes. The Debye temperature (Θ_D) is derived by the equation $\Theta_D = (12\pi^4 N k_B / 5\beta)^{1/3}$.

Fitting parameters	One Debye + one Einstein
ϕ (10^{-4} J mol^{-1} K^{-2})	6.90
β (10^{-5} J mol^{-1} K^{-4})	9.32
A (J mol^{-1} K^{-1})	2.94
Θ_E (K)	83.13
Θ_D (K)	275
R^2	0.99997
χ^2	0.000000126

Table S5 Parameters used to fit the lattice thermal conductivity of $Cu_7Sn_3S_{10}$.

Fitting parameters	$Cu_7Sn_3S_{10}$
L (μm)	0.53
A (10^{-41} s^3)	0.603
B (10^{-18} s K^{-1})	11.265
C (10^{36} s^{-3})	4.541
ω/v (THz)	10.9/1.73
R^2	0.99828
χ^2	0.02738

*ω is angular frequency and v is frequency, and their units are the same THz. (i.e. $\omega=2\pi v$)
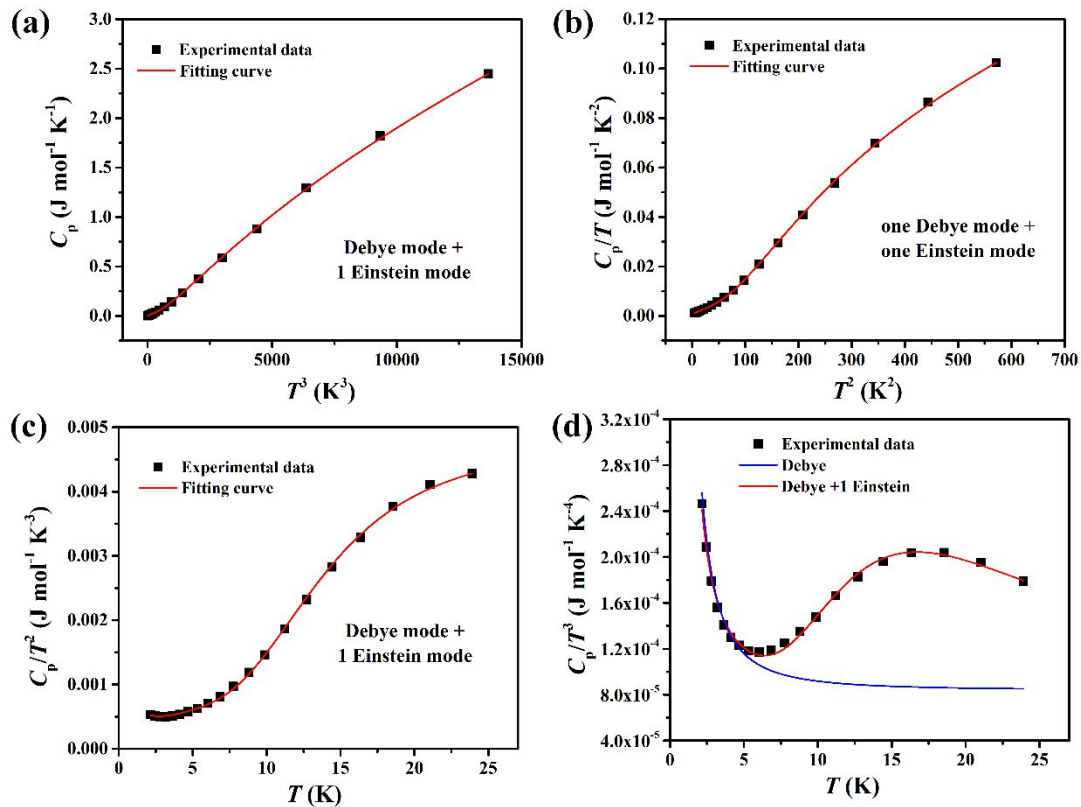
Fig. S1 Heat capacity fitting for $Cu_7Sn_3S_{10}$ from 2 to 25 K. (a-c) C_p versus T^3, C_p/T versus T^2, and C_p/T^2 versus T for $Cu_7Sn_3S_{10}$ by using one Debye mode + one Einstein mode. (d) C_p/T^3 versus T for $Cu_7Sn_3S_{10}$ from 2 K to 25 K fitted by Debye mode and one Debye mode + one Einstein mode, respectively.
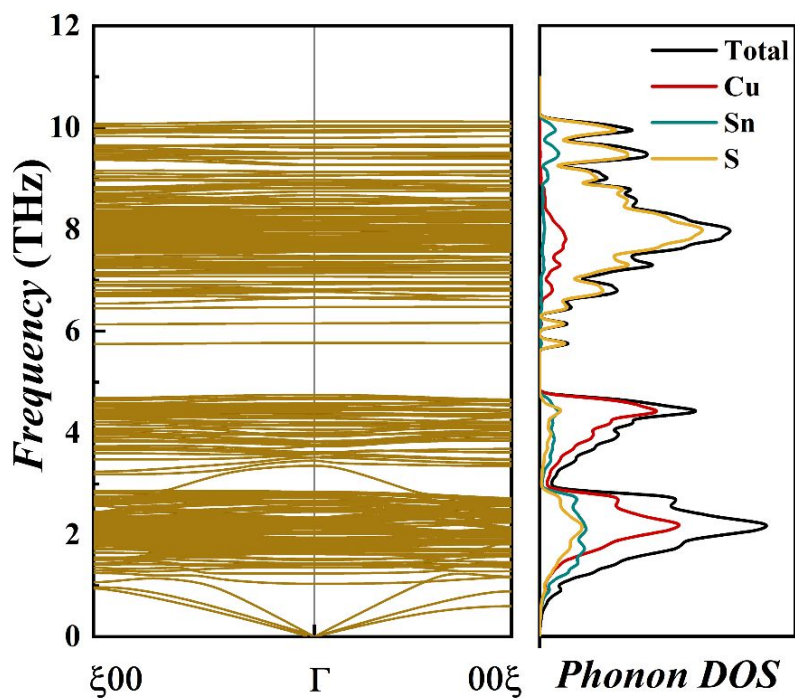
Fig. S2 Phonon dispersions and projected phonon density of states for $Cu_7Sn_3S_{10}$.

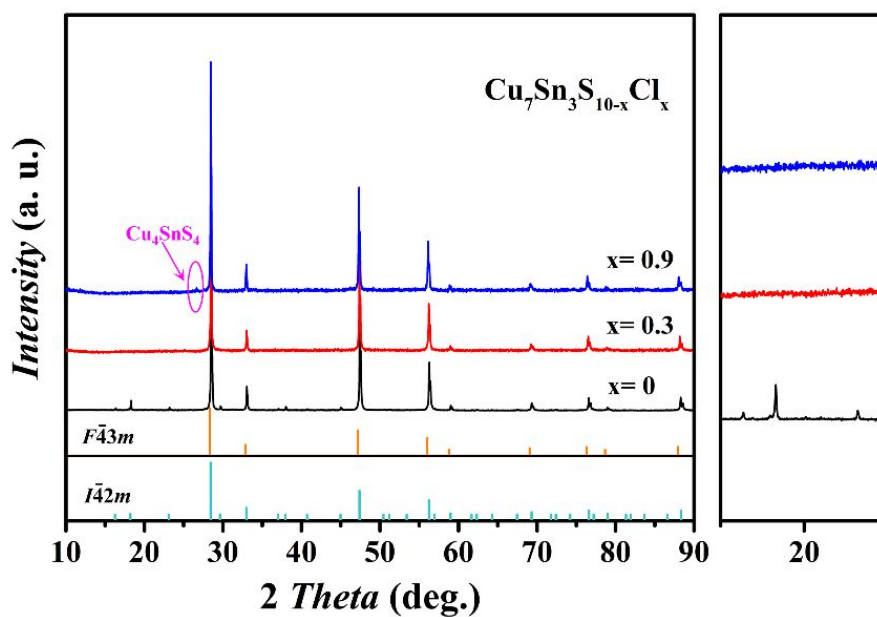**Fig. S3** Powder X-ray diffraction patterns for $Cu_7Sn_3S_{10-x}Cl_x$ (x=0, 0.3, and 0.9) samples. The appearance of diffraction peaks belonging Cu_4SnS_4 indicates that the Cl-doping content in $Cu_7Sn_3S_{10}$ is less than x = 0.9.

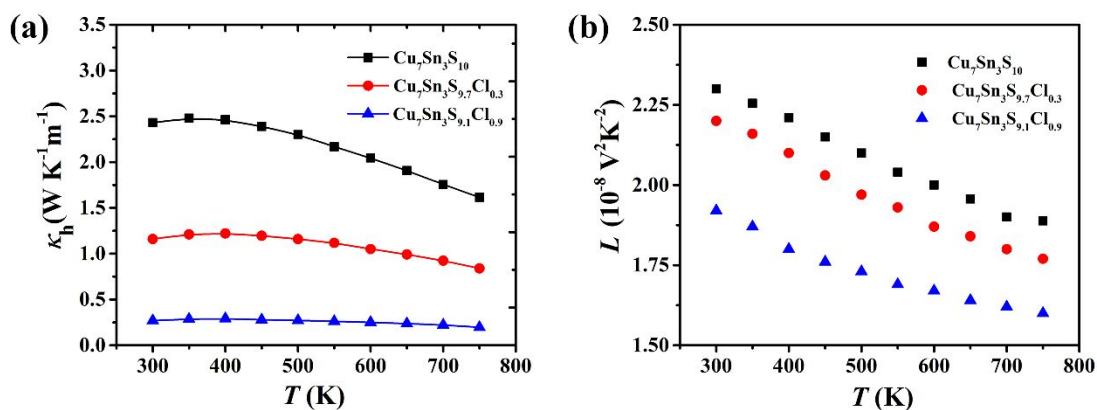**Fig. S4** Carrier thermal conductivity (κ_h) and Lorenz number (L) derived by the single parabolic band model for $Cu_7Sn_3S_{10}$, $Cu_7Sn_3S_{9.7}Cl_{0.3}$, and $Cu_7Sn_3S_{9.1}Cl_{0.9}$ samples from 300 K to 750 K.
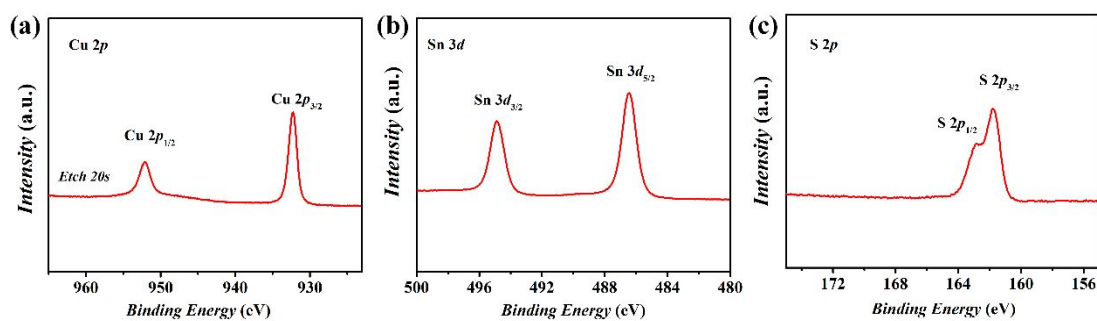

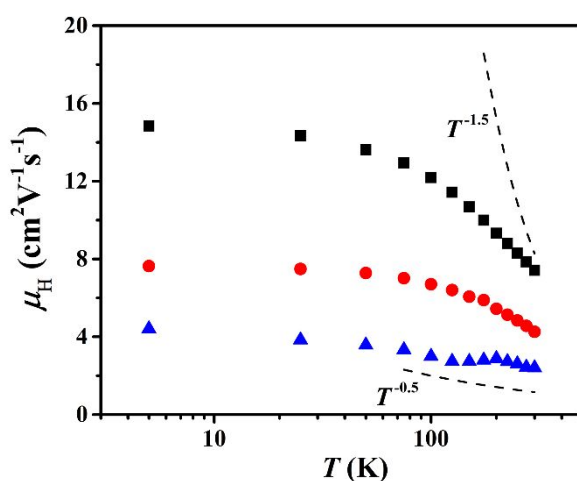**Fig. S5** XPS spectra of $Cu_7Sn_3S_{10}$: (a) Cu 2p, (b) Sn 3d, and (c) S 2p.

Fig. S6 Temperature dependence of Hall carrier mobility (μ_H) for $Cu_7Sn_3S_{10-x}Cl_x$ (x=0, 0.3, and 0.9) samples from 5 K to 300 K. The dashed lines represent the μ_H-$T^{-1.5}$ and μ_H-$T^{-0.5}$ relationships, respectively.
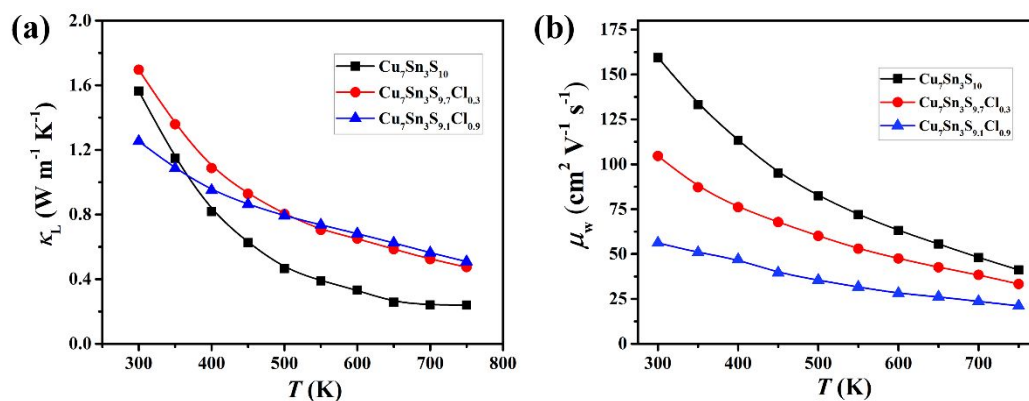
Fig. S7 (a) Lattice thermal conductivity κ_L as a function of temperature for $Cu_7Sn_3S_{10-x}Cl_x$. It decreases with temperature as expected from phonon-phonon scattering and is not strongly influenced by the Cl content. (b) The weighted mobility μ_w as a function of temperature for $Cu_7Sn_3S_{10-x}Cl_x$. It decreases with temperature as expected from phonon scattering and decreases with Cl content.

References

1.   G. Kresse and J. Furthmu¨ller, *Phys. Rev. B*, 1996, **54**, 11169-11186.

2.   P. E. Blochl, *Phys. Rev. B*, 1994, **50**, 17953-17979.

3.   J. P. Perdew, K. Burke and M. Ernzerhof, *Phys. Rev. Lett.*, 1996, **77**, 3865-3868.

4.   A. van de Walle, P. Tiwary, M. de Jong, D. L. Olmsted, M. Asta, A. Dick, D. Shin, Y. Wang, L. Q. Chen and Z. K. Liu, *Calphad*, 2013, **42**, 13-18.